

Numerical study on the influence of boundary-layer thickness on tip-leakage flow for a hydrofoil

Kenshiro Takahashi^{1*}, Patrick S Russell¹, Luka Barbaca¹, Bryce W Pearce¹, James A Venning¹ and Paul A Brandner¹

¹ Cavitation Research Laboratory, University of Tasmania, Launceston TAS 7250, Australia

*Emailto: kenshiro.takahashi@utas.edu.au

Abstract

This study numerically analyses the influence of boundary layer (BL) thickness on the tip-leakage flow for a stationary hydrofoil, presenting the effectiveness of computational predictions. The commercially available computational fluid dynamics (CFD) package Simcenter STAR-CCM+ 2302, which employs a finite-volume method solver, was adopted for the simulations. The $k-\omega$ shear stress transport (SST) turbulence model was adopted, and steady simulations were performed to evolve the computations. The distinct BL thicknesses were simulated by adjusting the boundary condition on the inlet of the computational domain. The computed trajectories of the tip-leakage vortex (TLV) agreed with those obtained in the experiment (Russell *et al.*, 2024). The leakage flow (transverse flow in the tip clearance) became more significant with decreasing the tip gap, supporting the shift of the TLV away the hydrofoil suction face. The incipient cavitation numbers predicted with CFD for the thicker BL ($\delta_{99} = 70$ mm) were smaller than those for the thinner BL ($\delta_{99} = 30$ mm), which was consistent with the decreased cavitation event rates with increasing BL thickness reported in the experiment. A high turbulence region extended downwards for the thicker BL, and more significant interactions of the TLV with the BL flow yielded. The higher ambient turbulence and interactions with the BL flow induced fluctuations of the TLV trajectories for the thicker BL and increased the pressure near the vortex core due to the interruption of the TLV coherence.

1 Introduction

Ducted propellers are expected to provide hydrodynamic and hydroacoustic advantages for underwater vehicles compared to conventional open propellers. However, an additional critical issue is raised due to its mechanical structure: ducted propellers possess a tip gap, also recognised as a tip clearance, between the blades and the duct surface. The tip gaps of such propellers can cause flow instability and global pressure minimum, resulting in undesirable cavitation. Therefore, tip-leakage flows (TLFs) have been studied to manage the hydroacoustics of ducted propulsors. Yongle *et al.* (2015) performed computational fluid dynamics (CFD) simulations to analyse the underlying mechanisms of the tip clearance effects for a ducted propeller, and reported that the vortex structure changed from multiple shedding vortices into a single enlarged separation vortex with an increase in the tip clearance. Villa *et al.* (2020) analysed the flow features of ducted and unducted propellers using a Reynolds-averaged Navier–Stokes (RANS) solver. They reported that the duct generated secondary vortices interacting with the primary tip vortex from the rotating blades, suggesting possible effects on the propeller noise and vibrations. Lv *et al.* (2022) computed the tip-leakage vortex (TLV) cavitating flow in a waterjet pump using a delayed detached eddy simulation. They clarified that the vortex evolution was divided into three stages: the tip-separation vortex (TSV) and the TLV developed independently during the first stage, the TSV approached and gradually merged into the TLV during the second stage, and the induced vortex developed and interacted with the TLV during the third stage. Guo *et al.* (2023) investigated the scale effect of the pump-jet propulsors using unsteady RANS simulations. The intensity of the TLV for the full-scale was smaller than that for the model scale, and the consequent interaction with the inner wall vortex of the duct was weakened.

Tip leakage flows have also been studied using a hydrofoil to analyse the fundamental phenomena under a stationary condition. Zhao *et al.* (2021) conducted experimental and numerical analyses of the tip-leakage cavitating flow for a hydrofoil. They reported that the cavitating flow for the NACA66 (mod) hydrofoil can be divided into three patterns governed by the angle of attack and cavitation number. Qian *et al.* (2022) performed a large-eddy simulation (LES) to analyse the unsteady tip-leakage cavitating flow of a stationary hydrofoil. The computed cavity shapes visualised with the iso-surface of the vapour volume fraction and velocity distributions were consistent with the experimental results. Furthermore, the cavity interfacial oscillations were highly



correlated with the surrounding velocity fluctuations. Ji *et al.* (2023) computed the cavitation noise in a TLF using LESs and the Ffowcs-Williams and Hawkings analogy for distinct tip-gap heights. A large amount of noise was generated with an increase in the tip gap, particularly in the high-frequency band. Furthermore, wavelet analysis indicated that the main broadband noise source for TLV cavitation inception was the multiple collapses of the cavitating bubbles. Feng *et al.* (2023) used a detached eddy simulation to analyse the cavitation inception for a hydrofoil, varying the tip-gap height. A smaller gap resulted in increased vorticity in both the TSV and TLV, reducing the pressure and thus increasing the incipient cavitation numbers. Chen *et al.* (2023) investigated the effect of the tip-edge fillet on the pressure drop in TLF. They concluded that the tip-edge fillet mitigated the pressure drop in the TSV due to the weakened velocity gradient. However, the fillet increased the pressure drop in the TLV because the velocities in the gap region accelerated. Chen *et al.* (2024) investigated the tip-leakage cavitating flow of twisted hydrofoils with the angle of attack (skew) smoothly varying in the spanwise direction. The tip-vortex cavitation presented cyclic oscillations with intermittent break-off and desinence for the lower-skew hydrofoil, whereas it showed continuous behaviour for the larger-skew hydrofoil.

In this context, experimental works on TLFs and relevant cavitation using stationary hydrofoils have been conducted to clarify the underlying physical phenomena at the University of Tasmania (UTAS) variable-pressure water tunnel. Russell *et al.* (2020) performed an experiment of a cavitating flow for a square-tipped hydrofoil. A TSV formed in the clearance flow from the sharpened end of the hydrofoil. The TSV and bubbles swept across the end of the hydrofoil by the leakage flow and wound around the TLV. Russell *et al.* (2022) developed a tool to design a hydrofoil geometry with faired endwall edges to suppress flow separation in the tip gap. The cavitation associated with shedding flow on the pressure side was not observed for the evaluated incident angles. Thereafter, the influence of boundary-layer (BL) thickness on incipient and developed cavitation in a stationary TLF was investigated experimentally using the faired hydrofoil (Russell *et al.*, 2024). Example TSV and TLV for a stationary hydrofoil are presented in Figure 1. The present CFD study was performed to acquire complementary flow field information and to test the effectiveness of computational predictions. Experiments (Russell *et al.*, 2024) revealed that the overall sound pressure levels and cavitation event rates decreased with increasing BL thickness on the test-section ceiling. Furthermore, the cavitating tip vortex trajectories have greater spanwise fluctuation downstream of the trailing edge for thicker BLs. Thus, this study numerically analyses the influence of BL thickness on the TLF for a stationary hydrofoil.

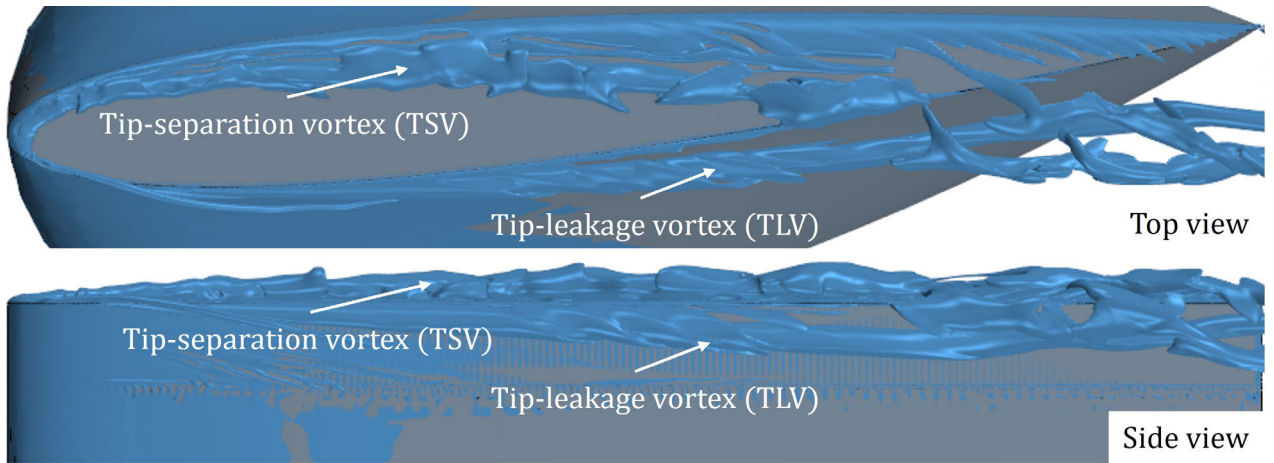


Figure 1. Schematic of TSV and TLV for a stationary hydrofoil as viewed from above (top) and side (bottom).

2 Computational setup

The test condition of the CFD simulations was based on the experiment of a cavitating flow for a hydrofoil at the UTAS variable-pressure water tunnel reported in Russell *et al.* (2024). The tunnel test-section is 0.6 m \times 0.6 m at the entrance and 2.6 m long. The hydrofoil, which had a chord (c) of 280 mm, was rigidly mounted to the bottom of the test section. The tip-gap height (h_g), which was the clearance between the hydrofoil tip and test-section ceiling, was varied from 3.36 mm to 67.2 mm. A gap ratio of $\tau = h_g/t = 0.1-2.0$ was obtained when non-dimensionalised by the maximum hydrofoil thickness ($t = 33.6$ mm). Experiments were performed at a hydrofoil incidence of $\alpha = 6.0^\circ$. The Reynolds number based on the hydrofoil chord (c) was

$Re_c = U_\infty c / \nu = 3 \times 10^6$, where U_∞ is the freestream velocity and ν is kinematic viscosity. Figure 2 shows the hydrofoil mounted in the test section. The hydrofoil leading edge was located 900 mm downstream of the test-section entrance. The origin of the xyz -coordinate system located at the intersection between the test-section centreline on ceiling and mid-chord of the hydrofoil, where x -axis was positive to the downstream and y -axis was positive upwards. The incident angle of the hydrofoil was adjusted about the y -axis. Figure 3 shows the computational domain modelling the UTAS tunnel. The computational domain consisted of the test and downstream sections, and the test-section entrance was used as the inlet boundary. Velocity, turbulence intensity and turbulent viscosity ratio distributions to model the distinct BL thicknesses were implemented to the inlet boundary, whereas a zero-velocity gradient and a constant pressure were applied to the outlet boundary. A no-slip condition was implemented to the test-section ceiling and hydrofoil surface, whereas a slip condition was implemented to the other tunnel walls.

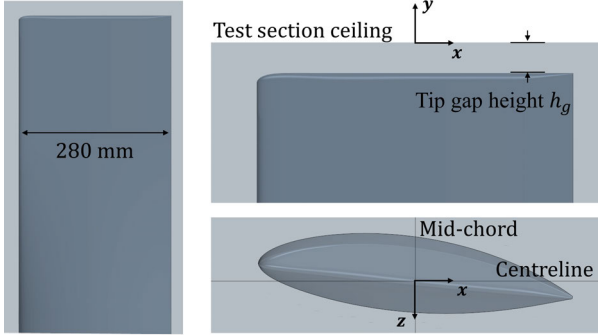


Figure 2. Hydrofoil mounted in test section.

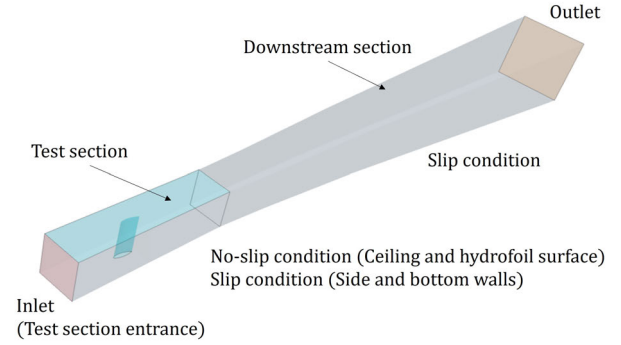


Figure 3. Computational domain modelling the UTAS tunnel consisting of test and downstream sections.

The commercially available CFD package Simcenter STAR-CCM+ 2302, which employs a finite-volume method solver, was adopted for the simulations. A second-order accuracy scheme was used for the spatial computation. The governing equations were determined using a segregated approach, and the semi-implicit method for pressure-linked equations (SIMPLE) algorithm was used to combine the pressure and velocity equations. The $k-\omega$ shear stress transport (SST) turbulence model was adopted (Menter, 1994), and steady simulations were performed to evolve the computations. The gamma transition model was adopted to predict the onset of the transition in a turbulent BL by solving an additional transport equation for turbulence intermittency (Menter *et al.*, 2015). The curvature correction approach was employed to incorporate the effects of rotation and curvature into the scalar eddy viscosity model (Arolla, 2013). An unstructured trimmed mesh was used to discretise the computational domain. Mesh refinement for the computational domain was performed in the test section, as shown in Figure 4. Prism layer meshes were generated on the tunnel wall to resolve the BL flow at an expansion ratio of 1.15. The nondimensional initial layer thickness of the prism layers on the test-section ceiling was ensured, i.e. $y_{\min}^+ = \Delta_{\min} \cdot u_\tau / \nu = 30$, where Δ_{\min} is the initial layer thickness [m] and $u_\tau (= \sqrt{\frac{1}{2} U_\infty^2 C_f})$ is the frictional velocity [m/s]. Here, C_f is the Schoenherr friction coefficient ($\frac{0.242}{\sqrt{C_f}} = \log_{10}(Re_l \cdot C_f)$), where Re_l is the Reynolds number based on the test-section length (l). Mesh refinement was additionally performed in the tip-gap region to compute the convoluted TLFs. Figure 5 shows the mesh configuration in tip-gap region determined based on a mesh convergence study. The total number of cells was approximately 86–123 million, which depended on the tested tip-gap height. Prism layer meshes were generated on the hydrofoil surface to ensure $y_{\min}^+ = 1.0$. Here, the Reynolds number based on the hydrofoil chord (Re_c) was used to calculate the Schoenherr friction coefficient (C_f).

3 Preliminary simulations for BL modelling

In the experiment (Russell *et al.*, 2024), a BL control system developed in Belle *et al.* (2016) adjusted the BL thickness on the test-section ceiling. Conversely, the distinct BL thicknesses were simulated by adjusting the boundary condition on the inlet of the computational domain. The boundary conditions (i.e. the xyz -velocity components, turbulence intensity and turbulent viscosity ratio) for modelling the intended BL thickness were obtained via preliminary simulations as follows:



Figure 4. Volume cells of computational domain.

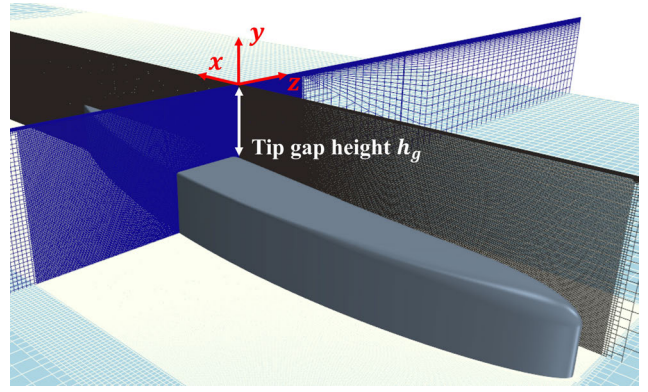


Figure 5. Volume cells near the tip-gap region.

1. The test section of the computational domain was extended upstream without modelling the hydrofoil. A uniform velocity distribution was applied to the inlet boundary for a natural BL development.
2. The computations were evolved to derive the BL thickness (δ_{99}) on the test-section ceiling at 700 mm downstream of the test-section entrance (200 mm upstream of the leading edge of the hydrofoil).
3. This sequence was iterated by changing the test-section extension to obtain a δ_{99} curve as a function of the extended length.
4. The extension lengths for simulating the intended BL thicknesses ($\delta_{99} = 30$ and 70 mm) were determined with interpolating the δ_{99} curve.
5. The test section was extended by the determined length for each δ_{99} , and computations were evolved.
6. The xyz -velocity components, turbulence intensity and turbulent viscosity ratio distributions on the plane at the test-section entrance location were extracted. Figure 6 shows the extracted x -axis velocity component (u_x) distributions for $\delta_{99} = 30$ and 70 mm.
7. The extracted physical values were applied to the inlet boundary of the computational domain for the subsequent TLF simulations.

Figure 7 shows the velocity distributions of the BL on the test-section ceiling at 700 mm downstream of the entrance (inlet) for $\delta_{99} = 30$ and 70 mm in the TLF simulations ($\tau = 0.8$). The velocity deficits recovered to $0.99U_\infty$ at $y \approx 30$ and 70 mm. However, the velocity deficits in the outer log region were slightly under-predicted when compared with a modified log-wake law (Guo *et al.*, 2005). Although the distance from the entrance to the sampled location could have been short for the BL to fully develop, further work will be required for improving the computational modelling.

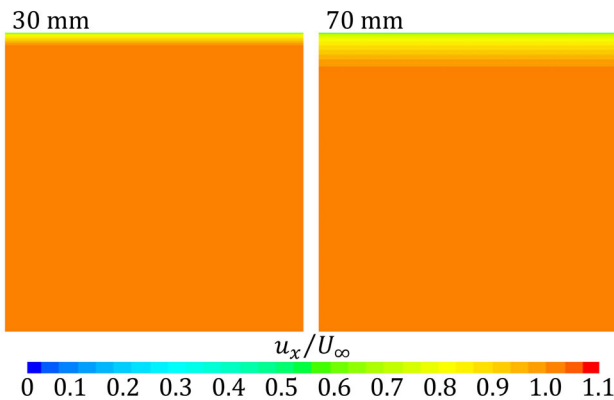


Figure 6. Extracted x -axis velocity component distributions for $\delta_{99} = 30$ and 70 mm.

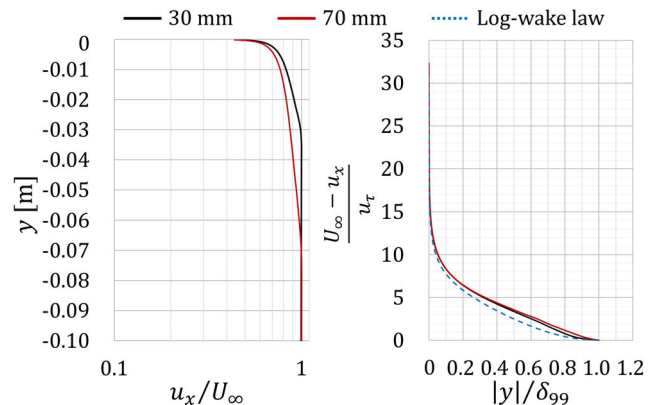


Figure 7. Velocity distributions of BL for $\delta_{99} = 30$ and 70 mm in TLF simulations ($\tau = 0.8$).

4 Results

Figures 8 and 9 depict the iso-surface of the Q-criteria ($Q = 1 \times 10^6 \text{ s}^{-2}$) for $\tau = 0.2, 0.6, 1.6$ and 2.0 for $\delta_{99} = 30 \text{ mm}$ and 70 mm with the superimposed 200 high-speed images presented in Russell *et al.* (2024). Here, the Q-criteria is defined as $Q = \frac{1}{2}(\|\Omega\|^2 - \|S\|^2)$, where $\|\Omega\|$ is the vorticity magnitude and $\|S\|$ is the strain rate magnitude. The computed TLV trajectories agreed with those obtained in the experiment: the TLV trajectory shifted away the suction face of the hydrofoil for the smaller gap, whereas the leakage vortex rolled up closer to the trailing edge for the larger gap. The difference in the TLV trajectories between $\delta_{99} = 30$ and 70 mm was insignificant. However, more small-scale vortices yielded and shed from the clearance at $\tau = 0.2$ and 0.6 for $\delta_{99} = 30 \text{ mm}$, which had a trivial influence on the TLV cavitation in the experiment. Figure 10 depicts the transverse (z -axis) velocity component contours (u_z / U_∞) at the slices perpendicular to the x -axis for $\delta_{99} = 30$ and 70 mm . The global velocity distribution unchanged for $\delta_{99} = 30$ and 70 mm . The larger z -axis velocity (leakage flow) was observed over the chord for $\tau = 0.2$. The greater velocity was still observed near the trailing edge at $\tau = 0.6$, whereas the velocity acceleration was insignificant at $\tau = 1.6$ and 2.0 . This flow field information supported that the leakage flow became more significant with decreasing the gap height and pushed the TLV away the hydrofoil.

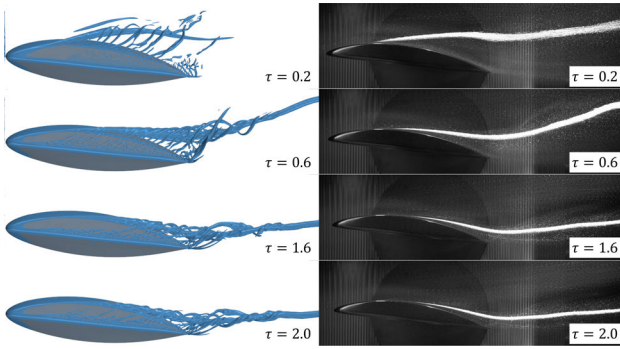


Figure 8. Plan view of TLV trajectories at $\tau = 0.2, 0.6, 1.6$ and 2.0 for $\delta_{99} = 30 \text{ mm}$.

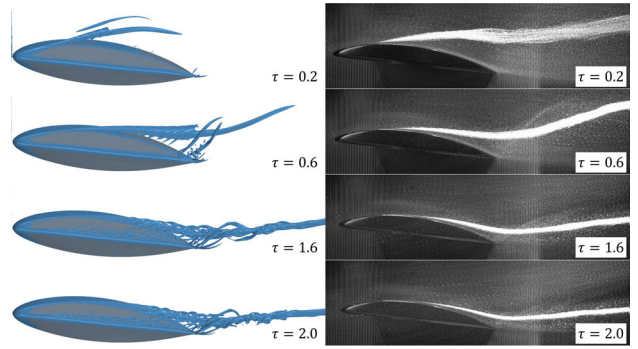


Figure 9. Plan view of TLV trajectories at $\tau = 0.2, 0.6, 1.6$ and 2.0 for $\delta_{99} = 70 \text{ mm}$.

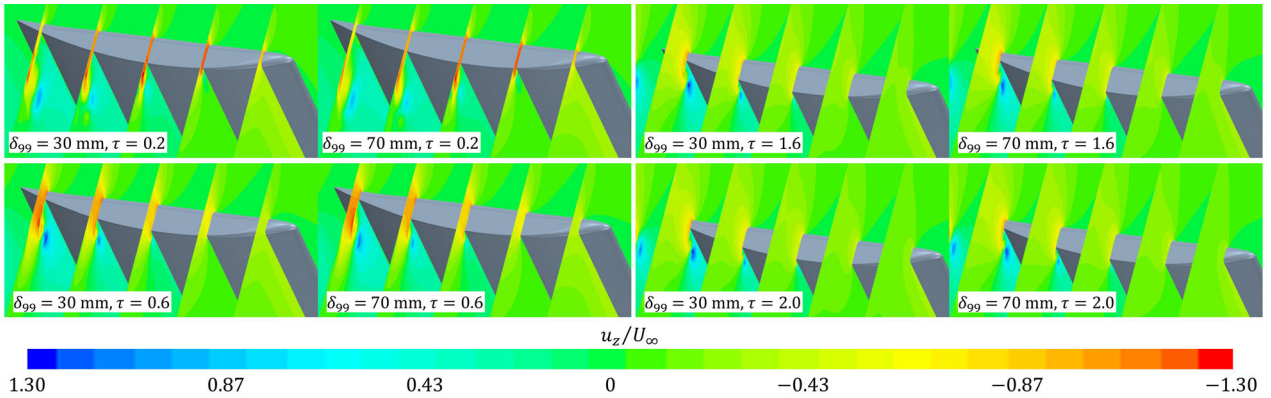


Figure 10. Transverse (z -axis) velocity contours (u_z) at slices perpendicular to the x -axis as viewed from suction side. Colour bar is inverted, which is negative in red.

Figure 11 shows the computed incipient cavitation numbers ($\sigma_i = -C_{P\min} = (p_{\min} - p_\infty) / \frac{1}{2}\rho U_\infty^2$) for $\delta_{99} = 30$ and 70 mm , where p_{\min} is the minimum pressure in the TLV, p_∞ is the ambient pressure and ρ is the water density. The computed σ_i for $\delta_{99} = 70 \text{ mm}$ was lower than that for $\delta_{99} = 30 \text{ mm}$, indicating the lower cavitation susceptibility with increasing BL thickness. Furthermore, σ_i for $\delta_{99} = 30 \text{ mm}$ increased with the decrease in τ and reached the maximum values at $\tau \approx 0.6-0.8$. Then, σ_i decreased significantly towards the lower τ . These results were consistent with the acoustic signature of cavitation inception obtained in the experiment (Russell *et al.*, 2024). Conversely, σ_i for $\delta_{99} = 70 \text{ mm}$ monotonically decreased with decreasing τ . The smaller difference in σ_i between $\delta_{99} = 30$ and 70 mm for the higher τ ($\approx 1.8-2.0$) indicated a less influence of the distinct BL thicknesses on the pressure drop in the TLV. Figure 12 shows the lift coefficients ($C_L = L / \frac{1}{2}\rho c^2 U_\infty^2$) for $\delta_{99} = 30$ and 70 mm , where L is the lift of the hydrofoil [N]. The lift force was computed by integrating the pressure

and shear stress on the entire hydrofoil surface. The difference in C_L was minor, whereas it monotonically increased with the decrease in τ . As a larger lift typically produces a greater leakage flow (i.e. accelerates a clearance flow) due to an increased differential pressure between the pressure and suction sides, σ_i can rise when the lift increases. However, the computed σ_i dropped after reaching the maximum value with decreasing τ , suggesting that the BL flow weakened TLV and mitigated the pressure drop near the vortex core.

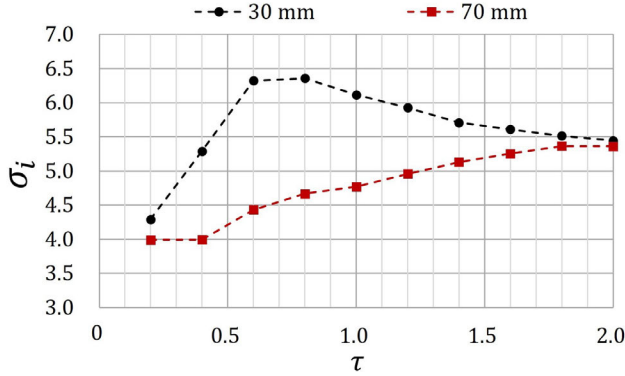


Figure 11. Computed incipient cavitation numbers (σ_i) for $\delta_{99} = 30$ and 70 mm.

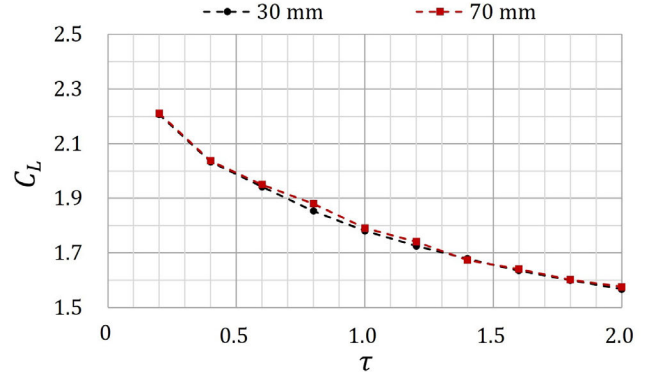


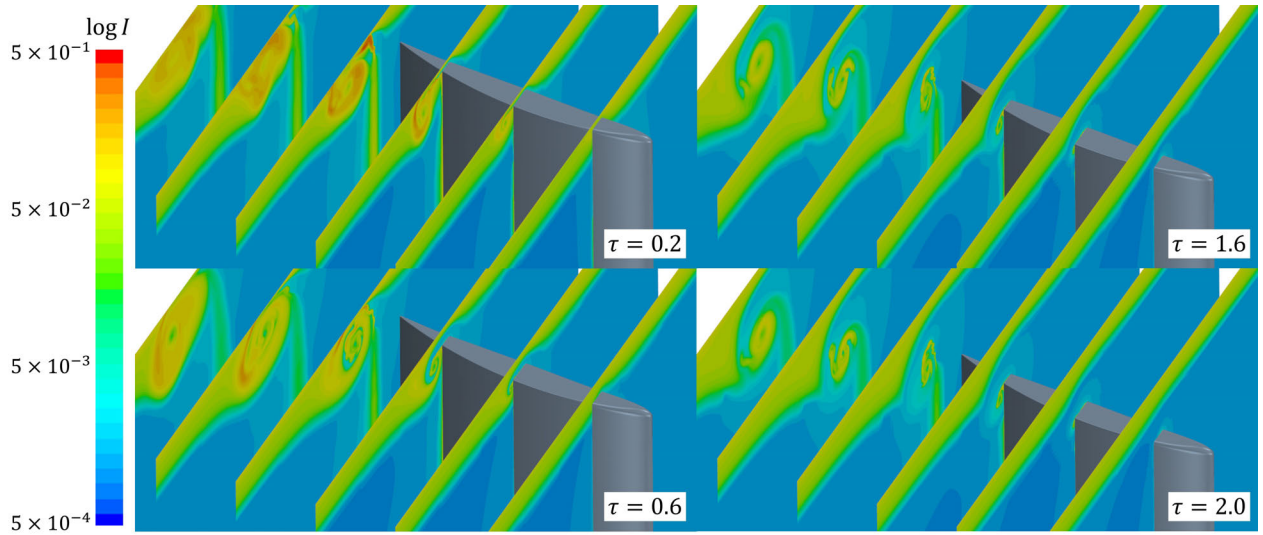
Figure 12. Computed lift coefficients (C_L) for $\delta_{99} = 30$ and 70 mm.

Figure 13 shows the turbulence intensity ($I = u' / U$) contours for $\tau = 0.2, 0.4, 0.8$ and 1.6 , where $u' (= \sqrt{\frac{2}{3}k})$ is the root-mean-square of the turbulent velocity fluctuations and $U (= \sqrt{u_x^2 + u_y^2 + u_z^2})$ is the mean velocity. Here, k and $u_{x,y}$ are the turbulence kinetic energy and x, y -axis velocity components, respectively. The higher I region extended downwards for the thicker BL. The TLVs were immersed in the BL at $\tau = 0.2$ for both $\delta_{99} = 30$ and 70 mm. Although the mainstream flow was slightly entrained in the TLV for $\delta_{99} = 30$ mm at $\tau = 0.6$, the TLVs were still immersed in the BL. More mainstream flow entered in the gap and existed between the TLV and BL at $\tau = 1.6$ and 2.0 for $\delta_{99} = 30$ mm. Conversely, the mainstream flow entering in the tip gap was limited for $\delta_{99} = 70$ mm, showing the rolling-up BL entrained by the TLV. These results supported that the higher turbulence and more interactions with the BL flow fluctuated the TLV trajectories for the thicker BL. Furthermore, the greater turbulence and interactions can disperse the TLV formation coherence, thus resulting in the mitigated pressure drop near the vortex core. In addition, these results made an assumption for the typical variation of σ_i as a function of τ . The pressure drop increases with decreasing τ due to the increased lift and resultant leakage flow for $\delta_{99} = 30$ mm. However, the BL influence became dominant for $\tau < 0.6$, mitigating the pressure drop due to the higher ambient turbulence. By contrast, the influence of the BL governed over the range of evaluated τ for $\delta_{99} = 70$ mm. Thus, the pressure drops for $\delta_{99} = 70$ mm were globally mitigated.

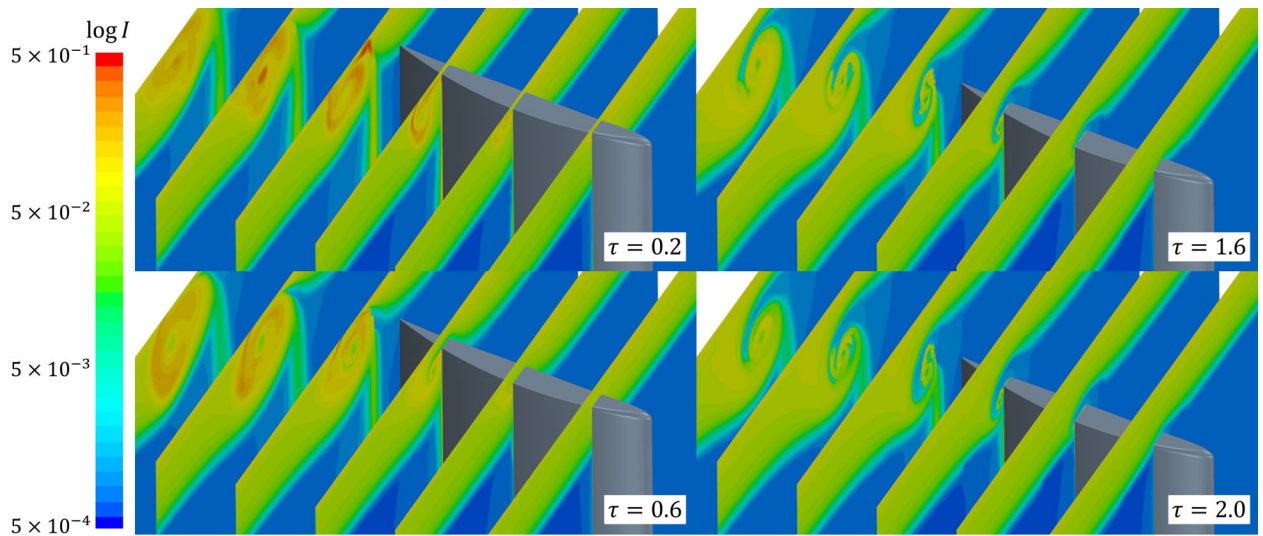
Figures 14 and 15 show the minimum pressure ($C_{P_{\min}}$) in the TLV at each plane perpendicular to the x -axis for $\delta_{99} = 30$ and 70 mm, respectively. Regardless of the distinct BL thicknesses, the x -axis location of the lowest $C_{P_{\min}}$ was constant: the lowest $C_{P_{\min}}$ was obtained at $x/c \approx -0.1$ for $\tau = 0.2$ and at $x/c \approx 0.5$ for the other evaluated τ . The upstream shift of the lowest $C_{P_{\min}}$ location at $\tau = 0.2$ was linked to the TLV upstream end shifting towards the hydrofoil leading edge. A significant difference was observed at $\tau = 0.6$: the lowest $C_{P_{\min}}$ for $\delta_{99} = 70$ mm was approximately 40% lower than that for $\delta_{99} = 30$ mm. Moreover, another peak of $C_{P_{\min}}$ existed downstream of the trailing edge (i.e. $x/c = 0.8$ at $\tau = 2.0$ for $\delta_{99} = 30$ mm and $x/c = 0.8-0.9$ at $\tau = 1.6$ for $\delta_{99} = 70$ mm). Chesnakas and Jessup (2003) remarked an incipient cavitation caused by an unsteady secondary vortical structure via the experiment using a ducted propeller. Thus, further investigation will be performed to analyse the pressure fluctuations caused by the secondary vortical structure for the hydrofoil using a detached eddy simulation.

5 Conclusions

A numerical study on the influence of BL thickness on TLF for a hydrofoil was presented. The computed TLV trajectories agreed with those obtained in the experiment. The leakage flow became more significant with decreasing the tip gap, supporting the shift of the TLV away the hydrofoil suction face. The incipient cavitation numbers predicted with CFD for $\delta_{99} = 70$ mm were smaller than those for $\delta_{99} = 30$ mm, which was consistent with the decreased cavitation-event rates with increasing BL thickness reported in Russell *et al.* (2024). The



(a) $\delta_{99} = 30 \text{ mm}$



(b) $\delta_{99} = 70 \text{ mm}$

Figure 13. Turbulence intensity (I) contours at slices perpendicular to the x -axis as viewed from suction side.

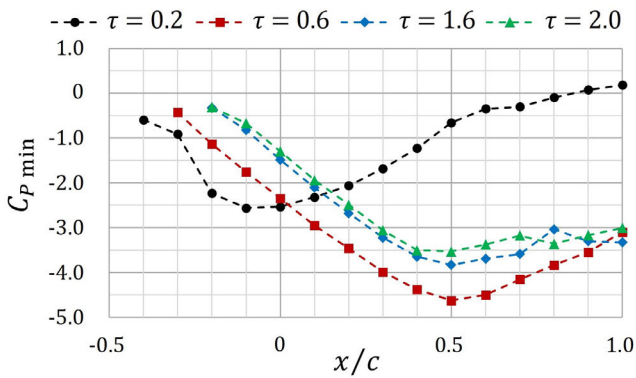


Figure 14. Minimum pressure coefficient of TLV at each x/c plane for $\delta_{99} = 30 \text{ mm}$.

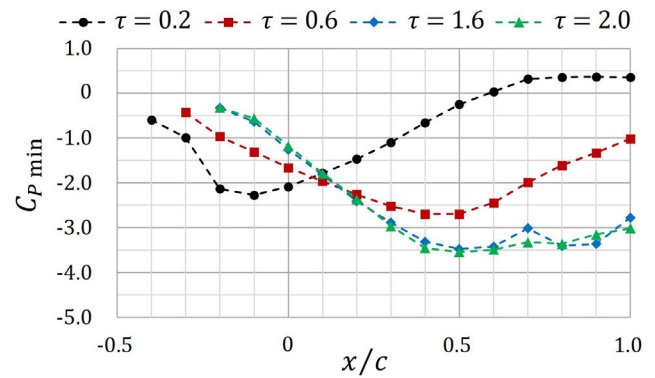


Figure 15. Minimum pressure coefficient of TLV at each x/c plane for $\delta_{99} = 70 \text{ mm}$.

higher turbulence region extended downwards for the thicker BL, and more significant interactions of the TLV with the BL flow yielded. The higher ambient turbulence and interactions with the BL flow supported the

fluctuations of the TLV trajectories for the thicker BL and the mitigated pressure drop near the vortex core due to the interruption of the TLV coherence. This research will be extended to analyse the pressure fluctuations caused by the secondary vortical structure using a detached eddy simulation.

Acknowledgments

This project was supported by the U.S. Office of Naval Research (ONR) Global through NICOP S&T Grant no. N62909-22-1-2058.

References

- Arolla, S.K. 2013, Modeling and eddy simulation of rotating and curved turbulent flows. PhD thesis, Iowa State University, Ames (IA).
- Belle, A., Brandner, P.A., Pearce, B.W., de Graaf, K.L. and Clarke, D.B. 2016, Artificial thickening and thinning of cavitation tunnel boundary layers, *Exp. Therm. Fluid Sci.*, **78**, 75–89.
- Chen, W., Xiang, Q., Li, Y. and Liu, Z. 2023, On the mechanisms of pressure drop and viscous losses in hydrofoil tip-clearance flows, *Energies*, **269**, 126712.
- Chen, Y., Liu, L., Li, J., Gong, Z. and Chen X. 2024, Large eddy simulation of tip-leakage cavitating flow around twisted hydrofoil with effects of tip clearance and skew angle, *Eur. J. Mech. - B/Fluids*, **103**, 25–42.
- Chesnakas, C.J. and Jessup, S.D. 2003, Tip-vortex induced cavitation on a ducted propulsor, in *Fluids Engineering Division Summer Meeting: FEDSM2003*, Honolulu, Hawaii, USA.
- Feng, X., Liu, Y., and Wang, B. 2023, Tip leakage flow structures and its influence on cavitation inception for a NACA0009 hydrofoil, *J Fluids Eng.*, **145**(5), 051203.
- Guo, C., Yang, C., Sun, C., Wang, C., Yao, H. and Lin, J. 2023, Numerical investigation of the scale effects of pump-jet propulsor with a pre-swirl stator, *Phys. Fluids*, **35**, 027115.
- Guo, J., Julien, P.Y. and Meroney, R.N. 2005, Modified log-wake law for zero-pressure-gradient turbulent boundary layers, *JHR*, **43**(4), 421–430.
- Ji, B., Wang, X., Bai, X., Cheng, H. and Peng X. 2023, Cavitation inception noise excited by a tip leakage vortex with various gap sizes: A Eulerian–Lagrangian investigation, *Phys. Fluids*, **35**(12).
- Lv, S., Wang, X., Cheng, H. and Ji, B. 2022, Numerical investigation of tip leakage vortex cavitating flow in a waterjet pump with emphasis on flow characteristics and energy features, *Energies*, **15**(19), 6916.
- Menter, F.R. 1994, Two-equation eddy-viscosity turbulence models for engineering applications, *AIAA Journal*, **32**(8), 1598–1605.
- Menter, F.R., Smirnov, P.E., Liu, T. and Avancha, R. 2015, A one-equation local correlation-based transition model, *FTaC*, **95**, 583–619.
- Qian, Z., Wang, Z., Geng, C. and Luo, X. 2022, Vortex and cavity dynamics for the tip-leakage cavitation over a hydrofoil, *Phys. Fluids*, **34**(9).
- Russell, P.S., Barbaca, L., Venning, J.A., Pearce, B.W. and Brandner, P.A. 2020, Nucleation effects on tip-gap cavitation, in *Australasian Fluid Mechanics Conference: AFMC2020*, Brisbane, Australia.
- Russell, P.S., Barbaca, L., Venning, J.A., Pearce, B.W. and Brandner, P.A. 2022, The influence of nucleation on cavitation inception in tip-leakage flows, in *Symposium on Naval Hydrodynamics:SNH2022*, Washington, DC, USA.
- Russell, P.S., Takahashi, K., Barbaca, L., Venning, J.A., Pearce, B.W. and Brandner, P.A. 2024, The influence of boundary-layer thickness on incipient and developed cavitation in tip-leakage flow, in *Symposium on Naval Hydrodynamics:SNH2024*, Nantes, France.
- Villa, D., Gaggero, S., Tani, G. and Viviani, M. 2020, Numerical and experimental comparison of ducted and non-ducted propellers, *J. mar. sci. eng.*, **8**(4).
- Yongle, D., Baowei, S. and Peng, W. 2015, Numerical investigation of tip clearance effects on the performance of ducted propeller, *Int. J. Nav. Archit.*, **7**(5), 795–804.
- Zhao, X., Zhao, Y., Wu, Q. and Huang, B. 2021, Experimental and numerical analysis of tip leakage cavitating flow around a 3D NACA66 (mod) hydrofoil, *Ocean Eng.*, **241**, 110005.